2020 IEEE/RSJ International Conference on Intelligent Robots and Systems (IROS)
October 25-29, 2020, Las Vegas, NV, USA (Virtual)

Drive-Train Design in JAXON3-P and Realization of Jump Motions: Impact Mitigation and Force Control Performance for Dynamic Motions

Kunio Kojima[1] Yuta Kojio[1] Tatsuya Ishikawa[1] Fumihito Sugai[1] Yohei Kakiuchi[1] Kei Okada[1] Masayuki Inaba[1]

***Abstract*— For mitigating joint impact torques, researchers have reduced joint stiffness by series elastic actuators, reflected inertia by low gear ratios, and friction torque from drive-trains. However, these impact mitigation methods may impair the control performance of contact forces or may increase motor and robot mass. This paper proposes a design method for achieving a balance between impact mitigation performance and force control fidelity. We introduce an inertia-to-square-torque ratio as a new index for integrating the parameters of torque generation (motor continuous torque limits, gear ratios, etc.) and the parameters of impact mitigation (joint stiffness, reflected inertia, etc.). In the process, we make a hypothesis that a motor mass is negatively correlated with the ratio. Based on the hypothesis, we calculate a joint breakdown region of impact torques, joint stiffnesses, and motor masses. Finally, we decide the drive-train specifications of JAXON3-P and demonstrate that the proposed method provides high impact mitigation and force control capabilities through several experiments including the jumping motion of 0.3 m COG height.**

I. INTRODUCTION

Robots have been able to contact environments recently and there are a lot of studies about human-robot interactions, multi-contact motions, and so on. However, robots have difficulty in absorbing impact forces caused by landing feet. Although pneumatic and SEA robots [1][2] absorb impact forces by their intrinsic joint elasticity, their mechanical bandwidth is a little low for balance control. Other robots maintain dynamic balance by their high-bandwidth force control but jump only a few tens of millimeters high owing to their high mechanical stiffness [3]. Though one of the few exceptions is Boston Dynamics' Atlas New Generation [4], the details remain to be elucidated.

The difficulty in absorbing landing impact arises from the complicated relationships between joint stiffness, reflected inertia and actuator mass. In this paper, we analyze the relationships and propose a method for designing robots' drive-train specifications with high impact mitigation performance and force control fidelity. Based on the proposed method, we developed JAXON3-P (Fig. 1(a)), which is capable of high jumping motions and stabilizing its own balance during whole-body motions. We exhibit the validity of the proposed method through verification experiments for impact mitigation and force control capabilities.

[1]K. Kojima, Y.Kojio, T. Ishikawa, F. Sugai, Y. Kakiuchi, K. Okada, and M. Inaba are with Graduate School of Information Science and Technology, The University of Tokyo, 7-3-1 Hongo, Bunkyo-ku, Tokyo 113-8656, Japan k-kojima@jsk.imi.i.u-tokyo.ac.jp

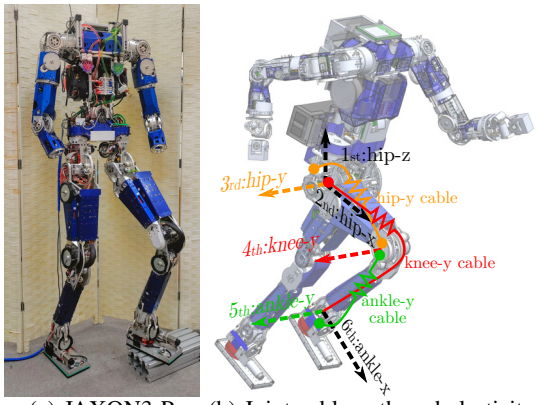

(a) JAXON3-P (b) Joint cable path and elasticity

Fig. 1: The appearance of JAXON3-P

II. CHALLENGES IN IMPACT FORCE MITIGATION DURING DYNAMIC MOTIONS

Difficulties in mitigating impact forces arise from low backdrivability of drive-trains. Obstructive factors of backdrivability are reflected inertia and friction torque. In previous studies, researchers have reduced or compensated for the factors by improving force control fidelity (Sec.II-A) and mechanical properties (Sec.II-B). In control approaches, robots are incapable of responding to external forces with higher bandwidth than that of controllers. In mechanical approaches, we have difficulty in achieving a balance between impact mitigation performance and force control fidelity because humanoid robots are required to absorb landing impacts while regulating contact forces for balance control. In the case of jumping motions, drive-train mass limitations impair design flexibility since landing impacts depend on a robot mass. Because of these difficulties, jump heights of life-sized humanoid robots with high control fidelity are under one hundred millimeters [3][5][6] except for Atlas[4].

A. Force Control Fidelity for Backdrivability

Researchers have studied force control methods by using force sensors. Hogan et al. proposed a method for controlling contact forces by achieving the desired impedance of a general-purpose manipulator [7]. Ott et al. reduced apparent motor inertia by joint torque feedback [8]. Humanoid robot TORO has a torque sensor in each joint and good torque control capabilities [9]. These methods use force/torque sensors and have difficulties in tracking contact forces changing faster than the control bandwidth.

There are some studies for reducing friction torques arising from drive-trains. Tien et al. applied a disturbance observer

to friction compensation [10]. Nagamatsu et al. proposed a low-latency joint torque feedback control by estimating and compensating for torque frictions on a high-frequency control cycle of an FPGA on each motor driver [11].

B. Mechanical Properties for Backdrivability

Mechanical properties about backdrivability are joint stiffness, joint friction, and reflected inertia.

One approach is to reduce joint stiffness for separating actuator's output shafts from the dynamics of reflected inertia and joint friction by using series elastic actuators [12]. Laurin-Kovitz et al. proposed a programmable passive impedance for improving the performance of SEA [13]. SEAs are used in some robots [2] [14] [15]. Pneumatic actuators with joint elasticity are also effective for absorbing impact forces and some pneumatic robots jump some hundreds of millimeters high [1][16]. However, lower joint stiffness decreases bandwidth of force control and may deteriorate balance control performance. Therefore, we must consider the relation between joint stiffness and force control fidelity.

Another approach is to reduce joint friction. Akiyama et al. proposed an efficient and backdrivable planetary gear mechanism by optimizing the numbers of teeth and the profile-shift coefficients [17]. In the domain of hydraulic actuation, Hydra has achieved high backdrivability by using low-friction hydraulic joint mechanism EHA [18].

For impact mitigation, we are required to reduce reflected inertia. Wensing et al. reduced reflected inertia by combining large high-torque motors and low gear ratio transmissions [19]. They reported that motor dimensions have little effect on reflected inertia ignoring gears under constant motor mass condition. Large mass motors with high continuous torques decrease gear ratios and reflected inertias, but may increase landing impact forces because of their own large mass. Kim developed a cable-driven manipulator LIMS with low mass and high joint stiffness and succeeded in human-robot interaction with collisions and impacts [20]. He achieved them by mounting motors at the proximal link and reducing the arm's weight. In the case of jump motions, however, we are not able to separate drive-train masses from moving parts and must reduce the robot total mass.

Thus, since landing impact forces have a strong relationship with reflected inertia, joint stiffness, and actuator mass, it is difficult to achieve both force control fidelity and impact mitigation performance for whole-body dynamic motions.

C. Design Approach for Combining Impact Mitigation with Torque Generation

In this paper, we propose a design method of robot drive-trains with high impact mitigation performance and high force control fidelity. In general, impact forces depend on the parameters of impact mitigation (joint stiffness, reflected inertia, etc.). In the case of landing impacts, the mass limitation associates these parameters with the parameters of torque generation (motor continuous torque limits, gear ratio, etc.) as discussed in Sec.II-B. The proposed method formulate the criterion of the impact mitigation and torque generation parameters for absorbing given landing forces mechanically and maximize the joint stiffness based on the criterion and the torque limit of drive-trains. This raises force control fidelity to the utmost limit with enough impact mitigation performance as reducing motor mass.

We show the flow of the proposed design flow in Fig. 2. In Sec.III, we set landing conditions and analyze the dependence on the impact joint torque of joint stiffnesses, reflected inertias, and joint frictions. In Sec.IV, we introduce an inertia-to-square-torque ratio IT^2 as a new design index and we make a hypothesis that a motor mass is negatively correlated with the rate. Then we verify the hypothesis based on modeled motor's properties and actual motors' specifications. In Sec.V, we calculate a joint breakdown region of impact torques, motor masses, and joint stiffnesses by integrating the impact joint torque of Sec.III and the hypothesis of Sec.IV. By using the breakdown region, we decide motor specifications and the maximum joint stiffness of JAXON3-P's drive-trains in sequence. In Sec.VI, we evaluate the impact mitigation performance and the force control fidelity of JAXON3-P through some uniaxial tests and whole-body motion experiments. Finally, we present conclusions in Sec.VII.

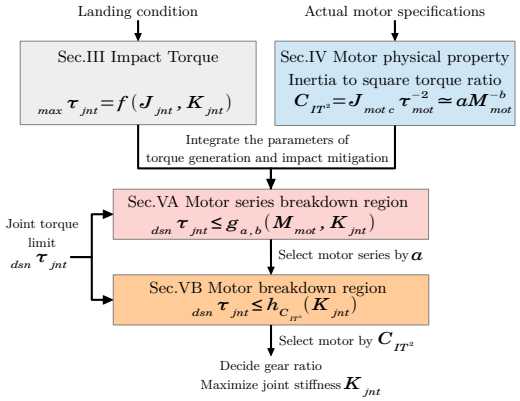

Fig. 2: Design flow using the inertia-to-square-torque ratio

III. IMPACT TORQUE CALCULATION ON A REDUCED LEG MODEL

This section studies the influence on impact torques of joint stiffnesses, reflected inertias, and joint frictions. We calculate the maximum joint torque on a reduced leg model as shown in Fig. 3. The model consists of a leg joint and a robot mass M. q and x denote joint angle and robot height respectively. The joint has a reflected inertia J_{jnt}, a joint stiffness K_{jnt}, viscous/dry joint frictions $D_{\mathrm{jnt}}\dot{q} + F_{\mathrm{jnt}}$, and a gear ratio N. The joint is connected to the link with a moment arm length l_{leg}. The dynamics of the model follow

$$M\ddot{x} = -Mg + \frac{\tau_{\mathrm{jnt}}}{l_{\mathrm{leg}}} \tag{1}$$

$$J_{\mathrm{jnt}}\ddot{q} = N\tau_{\mathrm{mot}} - \tau_{\mathrm{jnt}} \tag{2}$$

$$\tau_{\mathrm{jnt}} = K_{\mathrm{jnt}}(q - \frac{x}{l_{\mathrm{leg}}}) + D_{\mathrm{jnt}}\dot{q} + F_{\mathrm{jnt}} \tag{3}$$

where $\tau_{\rm jnt}$ and $\tau_{\rm mot}$ refer to a torque of the joint and the motor. Our purpose is to suppress the maximum joint torque ${}_{\max}\tau_{\rm jnt}$ when the robot lands on the ground at a velocity $v_{\rm land}$. We obtain the maximum joint torques ${}_{\max}\tau_{\rm jnt}$ by solving the above differential equation numerically for various combinations of $J_{\rm jnt}$, $K_{\rm jnt}$, and $D_{\rm jnt}$. We substitute $\tau_{\rm mot} \equiv 0$ for investigating mechanical passive properties. Assuming that $v_{\rm land}$ is the error of feet velocity at landing, $v_{\rm land} = -g\Delta T_{\rm land}$. $\Delta T_{\rm land}$ is the landing time error and 0.25 s. We apply $M = 35 = \frac{70}{2}$ kg and $l_{\rm leg} = 0.28 \simeq 0.4\sin(\frac{\pi}{4})$ m considering that the robot weighting 70 kg lands on its both feet with a length of 0.4 m. Fig. 4 shows the calculated maximum joint torques. Through preliminary experiments, we decided frictional parameters ($D_{\rm jnt} = 0.07$ Nms/rad and $Fj = 12.0$ Nm). The figure tells us that $D_{\rm jnt}$ and $F_{\rm jnt}$ are dominant around $K_{\rm jnt} < 100$ Nm/rad and that their dominance declines with an increase in $K_{\rm jnt}$.

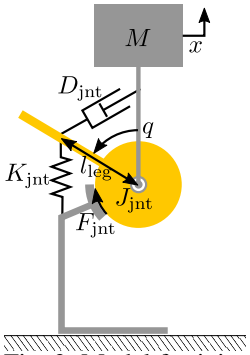

Fig. 3: Model for joint impact torque analysis

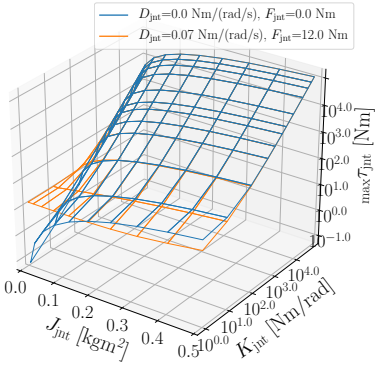

Fig. 4: Joint impact torque

IV. INERTIA-TO-SQUARE-TORQUE RATIO

A reflected inertia is dependent on a gear ratio and a motor rotor inertia and is little beneficial for selecting motors. Hence, we transform the maximum torques in Sec.III to the form dependent on motor masses. When we decide a gear ratio based on the continuous torques of a motor and a joint ($N = \frac{{}_{\rm cnt}\tau_{\rm jnt}}{{}_{\rm cnt}\tau_{\rm mot}}$), a reflected inertia is given as

$$J_{\rm jnt} = J_{\rm mot}N^2 = C_{\rm IT^2}\,{}_{\rm cnt}\tau_{\rm jnt}^2, \quad C_{\rm IT^2} := \frac{J_{\rm mot}}{{}_{\rm cnt}\tau_{\rm mot}^2}. \tag{4}$$

We define $C_{\rm IT^2}$ as the inertia-to-square-torque ($\rm IT^2$) ratio. The $\rm IT^2$ ratio is the coefficient of proportionality between $J_{\rm mot}$ and ${}_{\rm cnt}\tau_{\rm jnt}^2$ and depends on only motor properties. High-performance motors have a small $C_{\rm IT^2}$ in terms of impact mitigation. If the $\rm IT^2$ ratio is dependent on the motor mass, we are able to formulate the relation between the motor mass, the reflected inertia, and the joint torque ($J_{\rm mot} = C_{\rm IT^2}(M_{\rm mot})\ {}_{\rm cnt}\tau_{\rm jnt}^2$). By applying the formula to the results of Sec.III, we get a condition on motor masses and joint stiffnesses for absorbing impact torques. Therefore, we make a hypothesis that a motor mass is negatively related to a inertia-to-square-torque ratio. In the following subsections, we validate the hypothesis.

A. Model-based Validation of The Hypothesis

We extend the motor model of [21] for considering motors' Joule heat. The rotor and stator are approximated by a cylindrical geometry with a thin wall. The radial thicknesses of the rotor and stator are assumed to be constant ($t_{\rm r}$ and $t_{\rm s}$). The motor mass $M_{\rm mot}$, the rotor inertia $J_{\rm mot}$, and the stator surface area $S_{\rm s}$ are expressed as

$$M_{\rm mot} = 2\pi r_{\rm g} l_{\rm mot}(t_{\rm s}\rho_{\rm s} + t_{\rm r}\rho_{\rm r}) \tag{5}$$

$$J_{\rm mot} = 2\pi l_{\rm mot} t_{\rm r}\rho_{\rm r} r_{\rm g}^3 = \frac{t_{\rm r}\rho_{\rm r}}{t_{\rm s}\rho_{\rm s} + t_{\rm r}\rho_{\rm r}} r_{\rm g}^2 M_{\rm mot} \tag{6}$$

$$S_{\rm s} = 2\pi r_{\rm g} l_{\rm mot} = \frac{1}{t_{\rm s}\rho_{\rm s} + t_{\rm r}\rho_{\rm r}} M_{\rm mot} \tag{7}$$

where $r_{\rm g}$ is the gap radius and $l_{\rm mot}$ is the axial length. $\rho_{\rm s}$ and $\rho_{\rm r}$ are the density of the stator and rotor respectively. The gap radius of a motor is the radius of the magnetic interface between the rotor and the stator [21]. The maximum continuous motor torque ${}_{\rm cnt}\tau_{\rm mot}$ and current $I_{\max}$ follow

$${}_{\max}\tau_{\rm mot} \propto n l_{\rm mot} B r_{\rm g} I_{\max} \propto B l_{\rm wire} r_{\rm g} I_{\max} \tag{8}$$

where n is the number of wires in a cross-section perpendicular to the rotational axis, B is the field strength of the magnets, and $l_{\rm wire}(\propto n l_{\rm mot})$ is the total length of wire.

The maximum continuous current $I_{\max}$ depends on the ambient temperature $\rm T_0$ and the maximum winding temperature $T_{\rm th}$ as follows:

$$hS_{\rm s}(T_{\rm th} - T_0) = RI_{\max}^2 \Leftrightarrow I_{\max}^2 = \frac{h(T_{\rm th} - T_0)}{R} S_{\rm s} \tag{9}$$

where h is the average heat transfer coefficient. the wire mass $M_{\rm wire}$ and the resistance R is provided as

$$M_{\rm wire} \propto S_{\rm wire} l_{\rm wire} \propto 2\pi r_{\rm g} l_{\rm mot} t_{\rm s}\rho_{\rm s} = \frac{t_{\rm s}\rho_{\rm s}\ M_{\rm mot}}{t_{\rm s}\rho_{\rm s} + t_{\rm r}\rho_{\rm r}} \tag{10}$$

$$R \propto \frac{l_{\rm wire}}{S_{\rm wire}} \propto \frac{l_{\rm wire}^2}{M_{\rm wire}} \tag{11}$$

where $S_{\rm wire}$ is the cross-sectional area of each wire.

From Eq.(5)-Eq.(11), we obtain

$$C_{\rm IT^2} \propto \frac{\rho_{\rm r}(t_{\rm s}\rho_{\rm s} + t_{\rm r}\rho_{\rm r})}{B^2 h(T_{\rm th} - T_0)} \frac{t_{\rm r}}{t_{\rm s}} M_{\rm mot}^{-1}. \tag{12}$$

This indicates the dependence of the $\rm IT^2$ ratio $C_{\rm IT^2}$ on the motor mass $M_{\rm mot}$. Note that the values in Eq.(12) other than $M_{\rm mot}$ are constant in this model and that $C_{\rm IT^2}$ does not depend on $l_{\rm mot}$ or $r_{\rm g}$.

B. Data-based Verification of The Hypothesis

We investigated the relations between the $\rm IT^2$ rate $C_{\rm IT^2}$ and the motor mass $M_{\rm mot}$ based on data of about 150 actual motors. Fig. 5 shows the data collected from the TQ-RoboDrive ILM series, Maxon EC-4pole, EC-i, EC-max, and EC series and the regression curves $C_{\rm IT^2} = aM_{\rm mot}^{-b}$. The regression coefficients are shown in Table I. We excluded some special purpose motors for applications in oil, speed control, etc. $C_{\rm IT^2}$ of these series was found to be proportional to $M_{\rm mot}^{-0.71}$, $M_{\rm mot}^{-0.80}$, $M_{\rm mot}^{-0.56}$, $M_{\rm mot}^{-0.69}$, and $M_{\rm mot}^{-0.91}$. These coefficients are generally consistent with $M_{\rm mot}^{-1}$ in Eq.(12). The maximum correlation coefficient was 0.921. Though rotor/stator thickness invariance and housing/shaft mass would

increase modeling errors, these results validate the hypothesis that a motor mass is negatively correlated with an inertia-to-square-torque ratio C_{IT^2}. These are accurate and useful enough for studying impact mitigation performance.

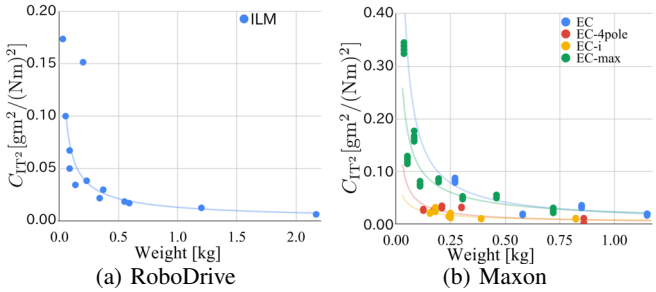

(a) RoboDrive (b) Maxon

Fig. 5: C_{IT^2} and M_{mot} from TQ-RoboDrive and Maxon

TABLE I: Estimated IT^2 rate $C_{\mathrm{IT}^2} = aM_{\mathrm{mot}}^{-b}$

Motor maker	Motor series	a	b
TQ-RoboDrive	ILM	1.3×10^{-5}	0.71
MAXON	EC-4pole	7.1×10^{-5}	0.80
	EC-i	7.6×10^{-5}	0.56
	EC-max	2.3×10^{-4}	0.69
	EC	2.2×10^{-4}	0.91

V. JOINT BREAKDOWN REGION OF MOTOR MASS AND JOINT STIFFNESS

A. Selection Criterion of Motor Series

We apply the relationships in Sec.IV-B to the maximum joint torque ${}_{\max}\tau_{\mathrm{jnt}}$ in Sec.III. In general, the design limit torque ${}_{\mathrm{dsn}}\tau_{\mathrm{jnt}}$ must satisfy ${}_{\mathrm{dsn}}\tau_{\mathrm{jnt}} := \alpha\ {}_{\mathrm{cnt}}\tau_{\mathrm{jnt}} > {}_{\max}\tau_{\mathrm{jnt}}$ $(\alpha \geq 1)$. Therefore, the mechanical drive-train will break when the following criterion is satisfied.

$$(M_{\mathrm{mot}},\ K_{\mathrm{jnt}},\ {}_{\mathrm{dsn}}\tau_{\mathrm{jnt}}) \tag{13}$$

s.t.

$${}_{\mathrm{dsn}}\tau_{\mathrm{jnt}} \leq {}_{\max}\tau_{\mathrm{jnt}}, \quad {}_{\max}\tau_{\mathrm{jnt}} = f(J_{\mathrm{jnt}}, K_{\mathrm{jnt}}) \tag{14}$$

$$J_{\mathrm{jnt}} = C_{\mathrm{IT}^2}\frac{{}_{\mathrm{dsn}}\tau_{\mathrm{jnt}}^2}{\alpha^2}, \quad C_{\mathrm{IT}^2} = aM_{\mathrm{mot}}^{-b} \tag{15}$$

$$J_{\mathrm{jnt}} \geq 0, \quad K_{\mathrm{jnt}} \geq 0, \quad M_{\mathrm{mot}} \geq 0 \tag{16}$$

The function $f(J_{\mathrm{jnt}}, K_{\mathrm{jnt}})$ denotes the calculation in Sec.III. a and b are the regression coefficients in Sec.IV-B.

Fig. 6 shows the breakdown regions of EC-4pole and EC-max ($\alpha = 1.5$). The sketches of these graphs are similar to each other. However, we are able to choose the joint stiffness of EC-4pole 5 to 10 times as large as that of EC-max. Fig. 7 shows the results with joint frictions ($D_{\mathrm{jnt}} = 0.07$ Nms/rad, $F_{\mathrm{jnt}} = 12.0$ Nm). These breakdown regions include some values around $M_{\mathrm{mot}} > 0.2$ and $K_{\mathrm{jnt}} < 100$, which are ${}_{\mathrm{dsn}}\tau_{\mathrm{jnt}} < 50$. This indicates that joint frictions have less effect on impact mitigation compared to joint stiffness.

The comparison between Table I and Fig. 6 tells us that the motor series with small a have small breakdown regions. Hence, we selected ILM, EC-4pole, and EC-i series with $a < 10^{-4}$.

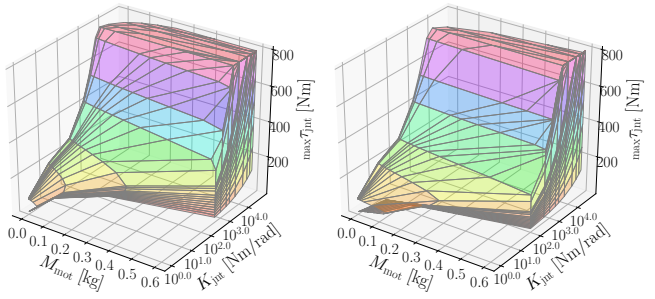

(a) EC-4pole (b) EC-max

Fig. 6: Breakdown regions without frictions ($D_{\mathrm{jnt}}, F_{\mathrm{jnt}} = 0$). Joint stiffnesses of EC-4pole are 5 to 10 times as large as that of EC-max.

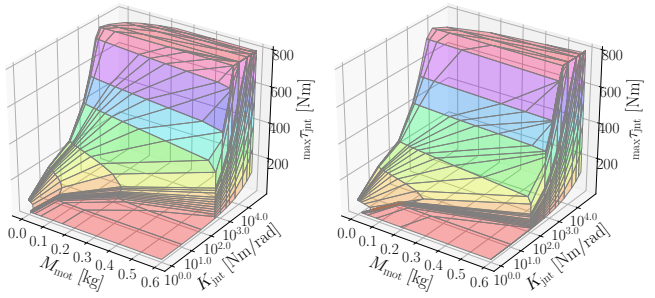

(a) EC-4pole (b) EC-max

Fig. 7: Breakdown regions of $D_{\mathrm{jnt}} = 0.07$ and $F_{\mathrm{jnt}} = 12.0$: Joint frictions have little effect compared to K_{jnt}.

B. Selection of Motors and Maximization of Joint Stiffness

Since a and b include regression errors in Sec.IV-B, we must calculate more accurately by using the data of a specific motor. We obtain the following accurate breakdown region from the specific motor's properties.

$$(K_{\mathrm{jnt}},\ {}_{\mathrm{dsn}}\tau_{\mathrm{jnt}}) \tag{17}$$

s.t.

$${}_{\mathrm{dsn}}\tau_{\mathrm{jnt}} \leq {}_{\max}\tau_{\mathrm{jnt}}, \quad {}_{\max}\tau_{\mathrm{jnt}} = f(J_{\mathrm{jnt}}, K_{\mathrm{jnt}}) \tag{18}$$

$$J_{\mathrm{jnt}} = \frac{J_{\mathrm{mot}}}{{}_{\mathrm{cnt}}\tau_{\mathrm{mot}}^2}\frac{{}_{\mathrm{dsn}}\tau_{\mathrm{jnt}}^2}{\alpha} \tag{19}$$

Fig. 8 shows the accurate breakdown regions of some motors of the series selected in Sec.V-A. These graphs show the data of the motors with a weight of around 150 to 850 g. ILM series frameless motors support high joint stiffness because excluding frame masses. In preliminary experiments, we found out that EC-4pole motor's continuous currents were 50 A with water cooling and added the data to Fig. 8(a). Fig. 8 tells us that

- small C_{IT^2} motors tend to support large joint stiffness.
- large and heavy motors tend to have small C_{IT^2}s.
- the difference between series larger than that within a series.
- water-cooled double motors support drastically large joint stiffness.

Water cooling have a great effect on shrinking the breakdown

area and EC-4pole 30 double motors with water cooling have the minimum IT^2 ratio $C_{\mathrm{IT}^2} = 1.58 \times 10^{-6}$ and obtain the maximum joint stiffness for the design value of the knee limit torque ${}_{\mathrm{dsn}}\tau_{\mathrm{jnt}} = 700$ Nm. Therefore, we selected the motor for JAXON3-P's knee joint and a joint stiffness $K_{\mathrm{jnt}} \simeq 8.5 \times 10^3$ Nm/rad with a little margin.Finally, a reference gear ratio is determined to 228 from ${}_{\mathrm{cnt}}\tau_{\mathrm{jnt}} = \frac{{}_{\mathrm{dsn}}\tau_{\mathrm{jnt}}}{\alpha}$ and ${}_{\mathrm{cnt}}\tau_{\mathrm{mot}}$.

Note that HarmonicDrives have too large joint stiffness (CSD20-100 $2.5{\times}10^4$[Nm/rad], CSD25-100 $4.7{\times}10^4$[Nm/rad], CSD32-100 $11{\times}10^4$[Nm/rad]) even when using water-cooled double motors.

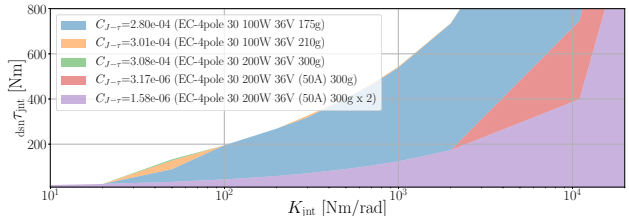

(a) EC-4pole

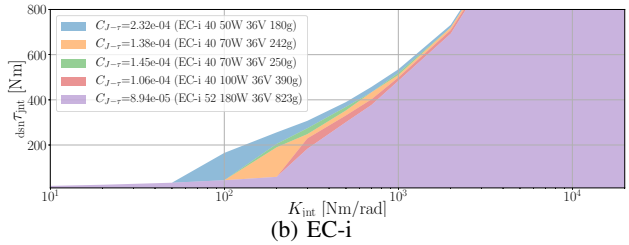

(b) EC-i

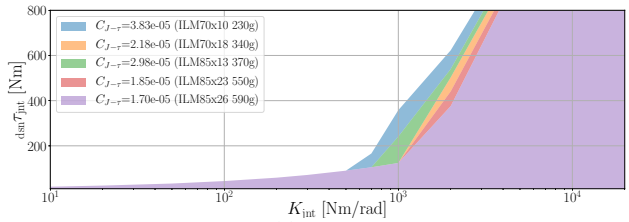

(c) ILM

Fig. 8: Breakdown regions of motors ($D_{\mathrm{jnt}}, F_{\mathrm{jnt}} = 0$)

VI. EXPERIMENTS AND VERIFICATION

A. Drive-train Specifications of JAXON3-P

Each joint's transmission of JAXON3-P consists of a gear transmission (the input stage) and a cable-pulley transmission (the output stage). These transmissions have one stage of reduction. The input and output gear ratios of the knee joint are 18:1 and 140:11 respectively. Some cables stretch over the thigh and shank link as shown in Fig. 1(b) for body weight-saving [22]. We achieve a target joint stiffness by adjusting a cable spring constant and a pulley diameter. For example, we selected the knee cable spring constant $1.7{\times}10^6$ N/m and the pulley diameter 0.14 m for $K_{\mathrm{jnt}} \simeq 8.5 \times 10^3$ Nm/rad. Table II shows the other joints' specifications.

B. Evaluation of Impact Mitigation Performance

We examine how large impact torque the joint compliance absorbs when JAXON3-P lands on the ground. We extended the real-time balance stabilizer of [23]. We replaced the foot force controller in [23] with a torque controller. The

TABLE II: Drive-train specifications of JAXON3-P

Joint	Joint Axis	Stiffness [Nm/rad]	Continuous torque [Nm]	Max velocity [deg/s]
Shoulder	y	3800	115	559
	x	4400	115	559
	z	2300	62	1040
Elbow	y	5600	96	672
Hip	z	4000	70	921
	x	29000	170	631
	y	8000	480	897
Knee	y	4700	516	832
Ankle	y	5900	85	762
	x	6300	74	869

torque controller calculates each joint reference torque from reference foot force/moments by inverse dynamics. The reference current of each joint is controlled by the following PD and current-based torque control.

$$i^{\mathrm{com}} = \frac{\tau^{\mathrm{ref}}}{NK_{\mathrm{tq}}} + P(\theta^{\mathrm{ref}} - \theta^{\mathrm{act}}) + D(\dot{\theta}^{\mathrm{ref}} - \dot{\theta}^{\mathrm{act}}) \quad (20)$$

K_{tq} denotes the torque constant. τ^{ref}, θ^{ref}, and $\dot{\theta}^{\mathrm{ref}}$ are the reference values of joint torque, position, and velocity from the whole-body control layer (frequency 500 [Hz]). A proportional gain P is 0.1 to 30 % of that in using only the PD controller. A derivative gain D is 1 to 70 %.

Fig. 10 shows the joint torques estimated from the motor current and the cable elongation ($\tau_{\mathrm{cur}} = N\tau_{\mathrm{mot}}$, $\tau_{\mathrm{cbl}} = K_{\mathrm{jnt}}(q - \frac{x}{l_{\mathrm{leg}}})$) during a jumping motion of 0.3 m COG height in Fig. 9. Since each joint of JAXON3-P has two angle encoders at the motor and the joint axis, we measure the cable elongation by the difference of the two encoder angles. We estimated $\tau_{\mathrm{dif}} = \tau_{\mathrm{cbl}} - \tau_{\mathrm{cur}}$ as the torques by joint inertia and frictions. The maximum τ_{dif} during the take-off and landing phase were about 120 Nm and 270 Nm respectively. The absorbed impact torques by the cable are considered to be about 150 Nm because the landing motion is almost the reverse-playbacked take-off motion. These results tell us that the joint compliance contributes significantly to landing impact mitigation.

The attached video includes the other experiments, where JAXON3-P jumps across the channel 0.47 m wide, jumps off a step 0.4 m high, and jumps over a rolling pipe.

C. Evaluation of Force Control Fidelity

1) Step Response Test on a Uniaxial Joint: We executed a step input test to identify the open-loop force control bandwidth. We set 0 to P and D in Eq.(20) and added 5 Nm step input to τ^{ref}. The current PI feedback control frequency of Eq.(20) is 41 [kHz]. Fig. 11 shows the result. The measured rising time is about 15 ms. The response bandwidth of the uniaxial joint is estimated to be about 23 Hz. This is low compared to the robots with HarmonicDrives. Because our force control is open-loop and does not use force sensor feedback, it has high enough control response at the whole-body balance controller layer as shown in Sec.VI-C.2.

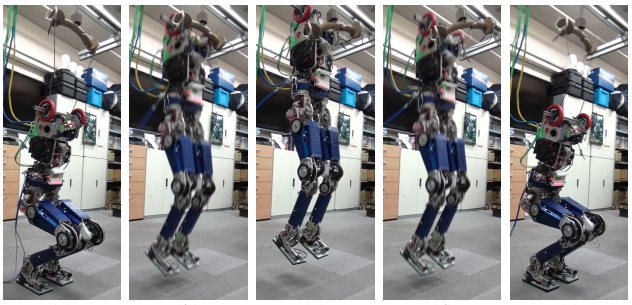

(a) (b) (c) (d) (e)

Fig. 9: Jumping Motion by JAXON3-P: The COG height is 0.3 m [22].

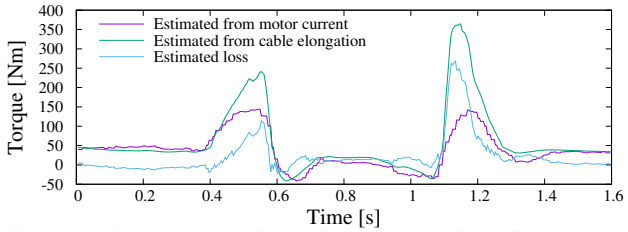

Fig. 10: Joint torque during a jumping motion of 0.3 m COG height: The gray area is the flight phase.

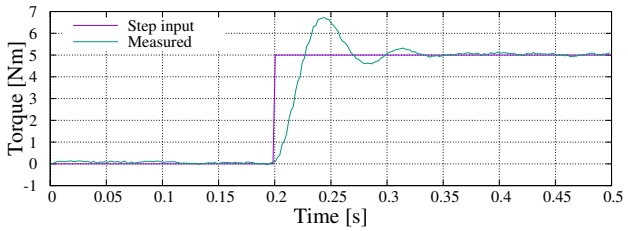

Fig. 11: Joint torque step response test

2) Response Test on a Whole-Body Balance Controller: We asses the influence of the control delay in Sec.VI-C.1 on a whole-body balance controller. In [23], Kajita et al. approximate the actual ZMP p lag behind the reference p^{com} by the first order lag in Eq.(21). They add a step input to p_{step} in Eq.(22), compare the responses between an experiment and a simulation on a linear inverted pendulum with the ZMP lag, and identify the time constant T_{p}.

$$p = \frac{1}{1 + sT_{\mathrm{p}}} p^{\mathrm{com}} \tag{21}$$

$$p^{\mathrm{com}} = p^{\mathrm{ref}} - k_{\mathrm{p}}(x - x^{\mathrm{ref}}) - k_{\mathrm{d}}\dot{x} - p_{\mathrm{step}} \tag{22}$$

We identify T_{p} in the same way. Fig. 12 shows the result of adding a step input p_{step} of 15 mm. We found out that $T_{\mathrm{p}} = 0.045$ s gives a good approximation. Since the time constant of HRP4-C and old JAXON[24] was respectively 0.05 [23] and 0.055, JAXON3-P has a high bandwidth control property of whole-body balance.

3) Walking Experiments on Uneven Terrain: We performed walking tests on uneven ground for evaluating whole-body balance control performance. We tested JAXON3-P to walk on small steps with a height of 30 mm. The robot was able to walk without any knowledge of the ground profile. Fig. 13 shows the trajectories of COM and ZMP. The only left foot steps on the gaps during the gray areas in Fig. 13.

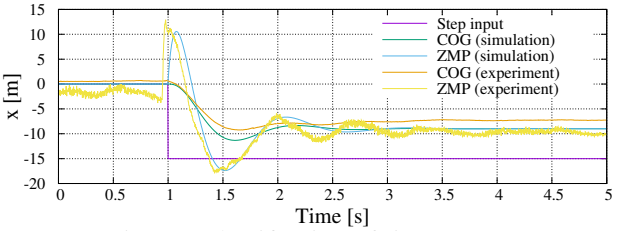

Fig. 12: Identification of time constant

For maintaining balance, the ZMP during the next right stance phase is modified to the right by the force control.

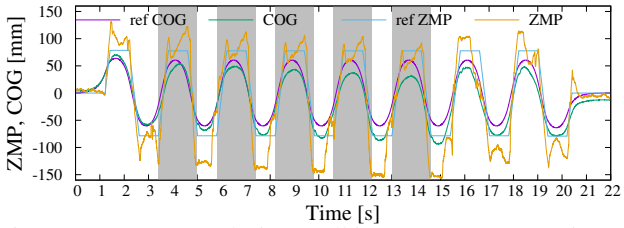

Fig. 13: ZMP/COG during walking on uneven terrain: The robot is walking on small steps with a height of 30 mm during gray areas. The ZMP is modified to the right during the next right stance phase.

D. Discussion

Robot body weight consists mainly of motors, frames, speed reducers, electric circuits, and batteries [22]. We refer readers to [25] for details of electric circuits and batteries subject power rather than torque. Little room is left for adjusting joint stiffness under constant design torque condition since the design limit torque ${}_{\mathrm{dsn}}\tau_{\mathrm{jnt}}$ is a main determinant factor of strength and stiffness of frames and speed reducers. Hence, we consider only the relation between motor mass and joint stiffness in this method. In addition, we ignored speed reducer inertia because it is small enough owing to gear ratio. For example, the reducer and motor reflected inertia of the JAXON3-P knee joint are $1.09 \times 10^{-4} \times (\frac{140}{11})^2 \simeq 0.018$ kgm^2 and $6.66 \times 10^{-6} \times 18^2 \simeq 0.35$ kgm^2 respectively.

For ease of explanation, we decided motor specifications, a gear ratio, and a joint stiffness from a design limit torque and a safety factor α in the proposed method. In practice, we fine-tune and decide these parameters with the constraint of breakdown regions owing to the constraints of a pulley diameter, a cable and gear strength, etc. The proposed method will be extended to encompass these factors in the future.

VII. CONCLUSIONS

In this paper, we proposed a design method of a humanoid robot capable of stable and dynamic motions by achieving high impact mitigation performance and high force control fidelity. In proposed methods, we proposed the inertia-to-square-torque ratio for calculating a joint breakdown region

of joint stiffnesses, motor masses, and joint impact torques. Based on the inertia-to-square-torque (IT^2) ratio and the breakdown region, we maximized the joint stiffness and decided the motor physical properties.

By analyzing breakdown regions, we made it clear that joint impacts vary between joint stiffnesses of HarmonicDrive® and those of actual cable-driven actuators. In that process, we verified the hypothesis about the inertia-to-square-torque ratio by the analysis of a motor model and large specification data sets. We found that the proportionality coefficient a and the IT^2 ratio are useful for selecting motor series and motors respectively. Then we have also found that water-cooled motors are effective for shrinking breakdown regions and raising joint stiffnesses. Finally, we designed the drive-train specifications of JAXON3-P and demonstrated that JAXON3-P has enough high impact mitigation capability and high bandwidth force control through several basic and application experiments including the jumping motion of 0.3 m COG height.

Therefore, we concluded that the proposed robot design method is able to achieve a balance between the impact mitigation performance and the force control fidelity by combining the impact mitigation parameters and the torque generation parameters.

REFERENCES

[1] R. Niiyama, S. Nishikawa, and Y. Kuniyoshi. Biomechanical approach to open-loop bipedal running with a musculoskeletal Athlete Robot. *Advanced Robotics*, Vol. 26, No. 3-4, pp. 383–398, 2012.

[2] M. Grebenstein, et al. The DLR hand arm system. In *Proceedings of the 2011 IEEE International Conference on Robotics and Automation*, pp. 3175–3182, May 2011.

[3] T. Takenaka, et al. Real time motion generation and control for biped robot -4th report: Integrated balance control-. In *Proceedings of the 2009 IEEE/RSJ International Conference on Intelligent Robots and Systems*, pp. 1601–1608, Oct 2009.

[4] Atlas. Boston Dynamics. https://www.bostondynamics.com/atlas.

[5] R. Tajima, D. Honda, and K. Suga. Fast running experiments involving a humanoid robot. In *ICRA2009*, pp. 1571–1576, May 2009.

[6] S. Kajita, et al. A running controller of humanoid biped hrp-2lr. In *Proceedings of the 2005 IEEE International Conference on Robotics and Automation*, pp. 616–622, April 2005.

[7] N. Hogan. Impedance control: An approach to manipulation: Part i - theory. *Journal of Dynamic Systems, Measurement, and Control*, Vol. 107, pp. 1–7, 1985.

[8] C. Ott, A. Albu-Schaffer, A. Kugi, S. Stamigioli, and G. Hirzinger. A passivity based cartesian impedance controller for flexible joint robots - part i: torque feedback and gravity compensation. In *Proceedings of the 2004 IEEE International Conference on Robotics and Automation*, Vol. 3, pp. 2659–2665 Vol.3, April 2004.

[9] J. Englsberger, A. Werner, C. Ott, B. Henze, M. A. Roa, G. Garofalo, R. Burger, A. Beyer, O. Eiberger, K. Schmid, and A. Albu-Schffer. Overview of the torque-controlled humanoid robot TORO. In *Proceedings of the 2014 IEEE-RAS International Conference on Humanoid Robots*, pp. 916–923, Nov 2014.

[10] L. Le Tien, A. Albu-Schaffer, A. De Luca, and G. Hirzinger. Friction observer and compensation for control of robots with joint torque measurement. In *Proceedings of the 2008 IEEE/RSJ International Conference on Intelligent Robots and Systems*, pp. 3789–3795, Sep. 2008.

[11] Y. Nagamatsu, T. Shirai, H. Suzuki, Y. Kakiuchi, K. Okada, and M. Inaba. Distributed torque estimation toward low-latency variable stiffness control for gear-driven torque sensorless humanoid. In *Proceedings of the 2017 IEEE/RSJ International Conference on Intelligent Robots and Systems*, pp. 5239–5244, Sept 2017.

[12] G. A. Pratt and M. M. Williamson. Series elastic actuators. In *Proceedings of the 1995 IEEE/RSJ International Conference on Intelligent Robots and Systems*, Vol. 1, pp. 399–406 vol.1, Aug 1995.

[13] K. F. Laurin-Kovitz, J. E. Colgate, and S. D. R. Carnes. Design of components for programmable passive impedance. In *Proceedings of the 1991 IEEE International Conference on Robotics and Automation*, pp. 1476–1481 vol.2, Apr 1991.

[14] N. G. Tsagarakis, S. Morfey, G. Medrano Cerda, L. Zhibin, and D. G. Caldwell. Compliant humanoid coman: Optimal joint stiffness tuning for modal frequency control. In *Proceedings of the 2013 IEEE International Conference on Robotics and Automation*, pp. 673–678, May 2013.

[15] F. Negrello, M. Garabini, M. G. Catalano, P. Kryczka, W. Choi, D. G. Caldwell, A. Bicchi, and N. G. Tsagarakis. WALK-MAN humanoid lower body design optimization for enhanced physical performance. In *Proceedings of the 2016 IEEE International Conference on Robotics and Automation*, pp. 1817–1824, May 2016.

[16] T. Takuma, S. Hayashi, and K. Hosoda. 3d bipedal robot with tunable leg compliance mechanism for multi-modal locomotion. In *Proceedings of the 2008 IEEE/RSJ International Conference on Intelligent Robots and Systems*, pp. 1097–1102, Sep. 2008.

[17] N. Akiyama and Y. Fujimoto. Highly efficient 2k-h compound planetary reduction gearbox using balancer. In *IECON 2019 - 45th Annual Conference of the IEEE Industrial Electronics Society*, Vol. 1, pp. 669–674, Oct 2019.

[18] H. Kaminaga, et al. Enhancement of mechanical strength, computational power, and heat management for fieldwork humanoid robots. In *Proceedings of the 2016 IEEE-RAS International Conference on Humanoid Robots*, pp. 786–793, Nov 2016.

[19] P. M. Wensing, A. Wang, S. Seok, D. Otten, J. Lang, and S. Kim. Proprioceptive actuator design in the MIT Cheetah: Impact mitigation and high-bandwidth physical interaction for dynamic legged robots. *IEEE Transactions on Robotics*, Vol. 33, No. 3, pp. 509–522, June 2017.

[20] Y. Kim. Anthropomorphic low-inertia high-stiffness manipulator for high-speed safe interaction. *IEEE Transactions on Robotics*, Vol. 33, No. 6, pp. 1358–1374, Dec 2017.

[21] A. Ananthanarayanan, M. Azadi, and S. Kim. Towards a bio-inspired leg design for high-speed running. *Bioinspiration & Biomimetics*, Vol. 7, No. 4, p. 046005, aug 2012.

[22] K. Kojima, et al. A robot design method for weight saving aimed at dynamic motions: Design of humanoid JAXON3-P and realization of jump motions. In *Proceedings of the 2019 IEEE-RAS International Conference on Humanoid Robots*, pp. 617–624, October 2019.

[23] S. Kajita, et al. Biped walking stabilization based on linear inverted pendulum tracking. In *Proceedings of the 2010 IEEE/RSJ International Conference on Intelligent Robots and Systems*, pp. 4489–4496, Oct 2010.

[24] K. Kojima, et al. Development of life-sized high-power humanoid robot JAXON for real-world use. In *Proceedings of the 2015 IEEE-RAS International Conference on Humanoid Robots*, pp. 373–380, November 2015.

[25] F. Sugai, K. Kojima, Y. Kakiuchi, K. Okada, and M. Inaba. Design of tiny high-power motor driver without liquid cooling for humanoid JAXON. In *Proceedings of the 2018 IEEE-RAS International Conference on Humanoid Robots*, pp. 1059–1066, 2018.